

# Calibrationless Parallel Imaging Reconstruction Based on Structured Low-Rank Matrix Completion

Peter J. Shin<sup>1,2</sup>, Peder E.Z. Larson<sup>1,2</sup>, Michael A. Ohliger<sup>1</sup>, Michael Elad<sup>4</sup>,  
John M. Pauly<sup>5</sup>, Daniel B. Vigneron<sup>1,2</sup>, Michael Lustig<sup>2,3</sup>

<sup>1</sup> Department of Radiology and Biomedical Imaging, University of California at San Francisco, San Francisco, California, USA

<sup>2</sup> The UC Berkeley - UCSF Graduate Program in Bioengineering, California, USA

<sup>3</sup> Department of Electrical Engineering and Computer Science, University of California at Berkeley, Berkeley, California, USA

<sup>4</sup> Department of Computer Science, Technion – Israel Institute of Technology, Haifa 32000, Israel

<sup>5</sup> Magnetic Resonance Systems Research Laboratory, Department of Electrical Engineering, Stanford University, Stanford, California, USA

Submission to: *Magnetic Resonance in Medicine*

Correspondence to:  
Michael Lustig  
506 Cory Hall  
University of California, Berkeley  
Berkeley, CA 94720  
TEL: (650) 725-57005  
E-MAIL: mlustig@eecs.berkeley.edu

*Running head: Auto-calibration parallel imaging reconstruction method without calibration data*

*Manuscript body word count: abstract (126), body (7145)*

## Abstract

A calibrationless parallel imaging reconstruction method, termed simultaneous auto-calibrating and  $k$ -space estimation (SAKÉ), is presented. It is a data-driven, coil-by-coil reconstruction method that does not require fully sampled calibrating signals. In SAKÉ, an under-sampled multi-channel dataset is structured into a single matrix and data reconstruction is formulated as a structured low-rank matrix completion problem. An iterative solution that implements a projection-onto-sets algorithm with singular value hard-thresholding is described. Reconstruction results are demonstrated for under-sampled, multi-channel Cartesian and non-Cartesian data with no calibration data. These exhibit excellent image quality comparable to those obtained with calibration data. Finally, improved image quality is demonstrated by combining SAKÉ with wavelet-based compressed sensing. This method could benefit MR applications where acquiring accurate calibration data is limiting or not possible at all.

## INTRODUCTION

Parallel imaging is a powerful method that utilizes multiple receiver elements for reduced scanning time in magnetic resonance imaging (MRI) (1). In this scheme, simultaneous signal receptions through spatially distributed coils provide data redundancy by means of sensitivity encoding. When the sensitivity encoding is applied in conjunction with gradient encoding, the amount of data necessary for proper image reconstruction is greatly reduced. This enables accelerated data acquisition, specifically, under-sampling of  $k$ -space data below the apparent Nyquist rate.

The various parallel imaging methods developed so far differ in the way they use sensitivity information to remove aliasing artifacts resulting from the under-sampling. Reconstruction techniques such as simultaneous acquisition of spatial harmonics (SMASH) (2) and sensitivity encoding (SENSE) (3) expect that the reception profiles from each coil element are known beforehand. However, explicit coil sensitivity measurements often require separate calibration scans, which increases the overall

acquisition time. Moreover, any inconsistency due to motion or small errors in the sensitivity estimation manifest as significant visual artifacts in reconstructed images (4). Auto-calibrating methods avoid the difficulties and inaccuracy associated with explicit estimations by deriving sensitivity information implicitly from auto-calibration signals (ACS). In general, ACS is embedded in acquired data as fully sampled center together with under-sampled higher frequency  $k$ -space regions. Joint estimation techniques, such as JSENSE (5) or non-linear inversion method (6), attempt to iteratively estimate both the coil sensitivities and image contents while imposing some smoothness constraints on the sensitivity profiles. Data driven auto-calibrating methods, such as generalized autocalibrating partially parallel acquisition (GRAPPA) (7) and iterative self-consistent parallel imaging reconstruction (SPIRiT) (8) to name a few, estimate linear relationships within the ACS data (i.e. calibration of GRAPPA or SPIRiT kernels) and enforce that relationship to synthesize data values in place of unacquired samples (i.e. data reconstruction).

However, there are many cases in which acquiring sufficient ACS for accurate calibration is limiting or not possible at all. For example, in spectroscopic imaging, matrix sizes in spatial dimensions are relatively small and ACS acquisitions can take up a large portion of total imaging time. In the case of dynamic MRI, acquiring multiple ACS temporally is also time consuming. In non-Cartesian imaging, such as spirals, acquiring sufficient ACS requires longer readouts, which can result in artifacts due to off-resonance.

In this work, we developed an iterative parallel imaging reconstruction framework called SAKÉ (simultaneous auto-calibration and  $k$ -space estimation). It is a  $k$ -space based, coil-by-coil reconstruction method that does not require explicit calibration data. By using all acquired data samples efficiently, SAKÉ performs calibration and data interpolation simultaneously to synthesize a full  $k$ -space data set. In SAKÉ, much like SPIRiT and GRAPPA, it is the linear dependency in  $k$ -space that is exploited to reconstruct missing data. The difference, however, is that we estimate and impose the linear dependency simultaneously by organizing acquired data into a structured matrix, which consists of columns that are vectorized overlapping blocks in  $k$ -space (the same format can appear in GRAPPA/SPIRiT calibration as well). This matrix has low rank due to the linear dependency residing in multi-coil data (9, 10, 11). Therefore, the reconstruction is cast

into a structured low-rank matrix completion problem and is formulated as a constraint optimization. Low-rank matrix completion is an active area of research and is an extension of the compressed sensing theory to matrices (12). We adopted a projection-onto-sets type algorithm with singular value thresholding to solve the problem iteratively. SAKÉ can easily incorporate additional *a priori* information related to underlying MR images, such as sparsity (13) or phase constraints (14), for improved reconstruction performance, and can also be used with non-Cartesian sampled data.

In the following sections, we first review the  $k$ -space based parallel imaging reconstruction methods, GRAPPA/SPIRiT, and discuss the low-rank nature of a data matrix generated from multi-channel  $k$ -space data. We then formulate the SAKÉ reconstruction as a structured low-rank matrix completion, investigate outcomes of adopting different sampling patterns, and compare reconstruction performance with another auto-calibrating method, SPIRiT. In addition, we extend the method to incorporate compressed sensing by enforcing an additional sparsity constraint. Finally, we demonstrate reconstruction results from non-Cartesian (spirals) sampled data.

## Theory

### **$k$ -Space Based Parallel Imaging Reconstructions**

Coil profiles vary smoothly in image domain. This results in strong local correlations between  $k$ -space samples across all coils due to the Fourier convolution property. These local correlations, or linear dependencies, form the basis of auto-calibrating,  $k$ -space based methods like GRAPPA or SPIRiT. In the calibration step of GRAPPA/SPIRiT, the linear dependencies are estimated from ACS data by fitting so called GRAPPA/SPIRiT kernel weights. In the reconstruction process, assuming that the dependencies are the same everywhere in  $k$ -space, unacquired data samples are synthesized by applying the linear weights to their nearby  $k$ -space points across all coils. In the following, we represent the procedures in terms of linear equations.

The linear weights of GRAPPA/SPIRiT kernels can be easily estimated if we organize multi-channel ACS data into a single *calibration matrix* of which columns are vectorized data blocks selected by sliding a (multi-channel) window across the ACS. Here, the size of the window is chosen to equal the size of the kernels. A pictorial description of

constructing such a matrix is shown in Fig. 1a. Let  $A^{ACS}$  denote the calibration matrix. Then we can formulate the calibration process of estimating the linear weights into the following equation.

$$g_{ir}^H A^{ACS} = e_i^H A^{ACS} \quad [1]$$

Here,  $g_{ir}^H$  is a GRAPPA *kernel* (7) for  $i^{\text{th}}$  channel that contains linear weights and zeros in appropriate positions. These kernels are also determined by a specific sampling pattern indexed by  $r$ . The vector  $e_i$  is a vector from the canonical basis that simply selects a row in  $A^{ACS}$  of which linear combinations of neighboring data are being fitted to. We use the notation  $g_{ir}^H$  to denote the complex-transpose of  $g_{ir}$ . In the case of SPIRiT (8), linear coefficients for all surrounding samples are found regardless of the sampling pattern, and hence, the index  $r$  can be omitted from Eq. 1 to form a SPIRiT kernel  $g_i^H$ . By rearranging Eq. 1, we get

$$\begin{aligned} (g_{ir}^H - e_i^H) A^{ACS} &= 0 \\ (g_{ir} - e_i)^H A^{ACS} &= 0. \quad [2] \end{aligned}$$

In other words, GRAPPA/SPIRiT kernels (after subtracting out the vector  $e_i$ ) are left null space vectors of the calibration matrix  $A^{ACS}$ . Thus, we can view the calibration step as the process of finding a set of representative vectors in the left null space of  $A^{ACS}$ . Hereafter, we assume that the kernel size and the amount of the auto-calibrating data are chosen appropriately so as to guarantee that the matrix  $A^{ACS}$  has a non-trivial left null space, and hence, ensure that we can calibrate the GRAPPA/SPIRiT kernels.

As sensitivity encoding is a shift-invariant operation in  $k$ -space, the linear dependencies estimated from the ACS should hold throughout the entire  $k$ -space. We can formulate this statement into the following linear equations by extending Eq. 2 to

$$(g_{ir} - e_i)^H A = 0, \quad [3]$$

where  $A$  now denotes a *data matrix* of which columns consist of data blocks from the entire  $k$ -space as opposed to  $A^{ACS}$ , which only contains data samples from the auto-calibrating signals. Eq. 3 constitutes the most fundamental mechanism in GRAPPA/SPIRiT and provides the foundation for reconstructing unacquired data. It means that any (vectorized) data block in the  $k$ -space is *nulled* by the vector  $(g_{ir} - e_i)$  through the inner-product operation and the missing data points should be synthesized in such a way that fulfills this requirement (calibration consistency condition). When the

data matrix  $A$  is constructed with the under-sampled  $k$ -space dataset, many of its entries that correspond to the unacquired samples are now missing and are zero-filled. Then, the procedure of reconstructing a full  $k$ -space dataset is nearly equivalent to filling in the missing entries of the under-sampled data matrix. Thus, the aforementioned two-step GRAPPA/SPIRiT reconstruction can be viewed as 1) find a set of left null vectors of the calibration matrix  $A^{ACS}$  (Eq. 2), and 2) synthesize the missing entries in the data matrix  $A$  so that the left null vectors of the calibration matrix also become the left null vectors of the data matrix (Eq. 3). In PRUNO (9), the idea of estimating a set of vectors in the left null space is extended to identifying a basis that spans the left null space itself by performing singular value decomposition (SVD) on the calibration matrix. Then, again, missing data samples are synthesized so that  $k$ -space data blocks are jointly orthogonal to every element of the basis set. In this perspective, GRAPPA (7), SPIRiT (8) and PRUNO (9) methods can all be viewed as (left) null space formulations.

### Subspace View of Auto-calibrating Reconstruction

In this section, we now move our attention away from the left null space of the calibration matrix to its orthogonal complement, the column space (or range)  $\mathcal{R}(A^{ACS})$ . By definition, the column space  $\mathcal{R}(A^{ACS})$  is a subspace spanned by the columns of the calibration matrix  $A^{ACS}$ . In other words, every data block within the ACS lies in this subspace. Again, due to the shift-invariance of the sensitivity encoding operation, every vectorized data block from the entire  $k$ -space should also lie in the column space of the calibration matrix. Later in this section, we demonstrate this with an example. Thus, similar to the procedure discussed in the previous section, we can formulate the two-step reconstruction into 1) estimate the column space of the calibration matrix  $\mathcal{R}(A^{ACS})$  during the calibration step, and then 2) reconstruct a full data matrix  $A$  by enforcing every column of  $A$  to lie in that subspace. In the following sections, we give a mathematical formulation.

Let  $A^{ACS} \in \mathbb{C}^{m \times n}$  ( $m < n$ ) be a calibration matrix constructed from a calibration dataset with its SVD being

$$A^{ACS} = U \Sigma V^H \quad [4]$$

$$\begin{aligned}
&= [U_{\parallel} \quad U_{\perp}] \begin{bmatrix} \Sigma_k & 0 \\ 0 & \Sigma_{m-k} \end{bmatrix} \begin{bmatrix} V_{\parallel}^H \\ V_{\perp}^H \end{bmatrix} \\
&= U_{\parallel} \Sigma_k V_{\parallel}^H + U_{\perp} \Sigma_{m-k} V_{\perp}^H
\end{aligned}$$

Here,  $\Sigma$  is an  $m \times m$  diagonal matrix containing singular values in descending order,  $U$  and  $V$  are unitary matrices containing left and right singular vectors of  $A^{ACS}$ , respectively. We further decomposed  $U$  and  $V$  into two separate sub-matrices that correspond to  $k$  dominant singular values and non-dominant ones. Our intention is to estimate the basis that spans the column space of the calibration matrix  $A^{ACS}$  by  $U_{\parallel}$ , the dominant left singular vectors. From the perturbation theory of SVD, it is known that singular values and its corresponding left singular vectors are relatively insensitive to moderate perturbations made on the entries of a matrix (15). Consequently, we are approximating the column space basis of the noiseless calibration matrix by keeping only the dominant ones from the noisy calibration matrix. Once we have  $U_{\parallel}$ , we can define an orthogonal projection operator ( $P_{\parallel} = U_{\parallel} U_{\parallel}^H$ ) that projects any  $\mathbb{C}^{m \times 1}$  vector down to the subspace spanned by columns of  $U_{\parallel}$  (16, 17). If a vector  $x$  resides in that subspace, then  $P_{\parallel} x = x$  should hold. Thus, once the projection operator  $P_{\parallel}$  is estimated during the calibration step, the missing entries of the data matrix  $A$  should be synthesized to fulfill the calibration consistency condition  $P_{\parallel} A = A$ . This subspace-based formulation appears in the eigenvector approach to auto-calibrating parallel imaging reconstruction method (18).

To show that every data block in the entire  $k$ -space does lie in the estimated column space of the calibration matrix, we perform the following experiment with a fully sampled, 8-channel brain image with image size  $200 \times 200$ . First, a full data matrix  $A$  is constructed from the full  $k$ -space using a  $6 \times 6 \times 8$  window in  $k_x, k_y$  and coil dimension. Additionally, restricting calibration signal to be the center  $30 \times 30$  of the  $k$ -space data, a calibration matrix  $A^{ACS}$  is also constructed using the same window size. Then we calculate the SVD of  $A^{ACS}$ , identify the dominant singular values, and form a projection matrix ( $P_{\parallel}$ ) using the dominant left singular vectors  $U_{\parallel}$ . Then we *filter* the full data matrix  $A$  by projecting every columns of  $A$  down to the column space of  $A^{ACS}$  by calculating  $S = P_{\parallel} A$ . [5]

Here,  $S$  is the resulting data matrix we get after the projection operation and only has columns that are in the subspace spanned by the columns of  $U_{\parallel}$ . If the basis set  $U_{\parallel}$  does span the column space of the data matrix  $A$ , then we should get most of  $A$  back in  $S$ .

Additionally, we calculate

$$N = A - P_{\parallel}A, [6]$$

which is a matrix that contains filtered columns that lie in the subspace spanned by columns of  $U_{\perp}$ . Finally, we convert the data matrices  $S$  and  $N$  back into  $k$ -space datasets, Fourier Transform them into images and compare the results with images from the original  $k$ -space. How we revert a data matrix into a  $k$ -space dataset is discussed in detail in a later section.

Fig. 1b shows a square-root of sum-of-squares (SSoS) combined image of the center  $30 \times 30$  calibration data zero-padded to the original image size (top) and Fig. 1c shows the singular value distribution of the calibration matrix  $A^{ACS}$  (solid line). Note that the singular values decay rapidly and there is a clear separation between dominant singular values and insignificant ones. This shows that the calibration matrix has low rank and that a compact basis set can represent the column space  $\mathcal{R}(A^{ACS})$ . Out of 288 possible left singular vectors, we empirically chose 55 vectors ( $k = 55$ ) to form the basis set  $U_{\parallel}$  and evaluated Eq. 5 and Eq. 6 to get the matrices  $S$  and  $N$ , respectively. Fig. 2a clearly shows that the images corresponding to  $S$  are de-noised versions of the original images that correspond to  $A$ . Moreover, there are no visually noticeable signals left in the noisy images of  $N$ . However, when the value for  $k$  is under-estimated ( $k < 55$ ), as shown in Fig. 2b, the separation of the data into signal and noise becomes incomplete. This means that  $S$  (which we call a signal matrix) contains most of the signal component of the data matrix  $A$  when the basis set  $U_{\parallel}$  is estimated appropriately, and  $N$  (noise matrix) contains the noise part of  $A$ . Additionally, since the column space of  $S$  is spanned by a compact basis  $U_{\parallel}$ , the signal matrix  $S$  also has low rank just like the calibration matrix. Therefore, we conclude that there is a low-rank matrix  $S$  that closely represents the underlying MR signal when transformed back to  $k$ -space data form, and that (signal component of) every data block in the entire  $k$ -space does lie in the estimated column space of the calibration matrix. Thus, the previously mentioned subspace-based auto-calibrating method works. We will refer to the subspaces spanned by the columns of  $U_{\parallel}$  and  $U_{\perp}$  as signal subspace



and noise subspace, respectively. The additional information of the signal matrix  $S$  being low rank becomes crucial as we try to reconstruct a full  $k$ -space from an under-sampled dataset that does not have calibration signals.

### Structured Data Matrix

In this section, we further study the structural property of the data matrix. From a multi-channel data set with image size of  $N_x \times N_y$  and  $N_c$  number of coils, we can generate a data matrix  $A$  with the size of  $w^2 N_c \times (N_x - w + 1)(N_y - w + 1)$  by sliding a  $w \times w \times N_c$  sized (multi-channel) window across the entire  $k$ -space. For sufficiently large image size, the matrix will have more columns than rows. Moreover, due to the nature of the sliding-window operation, the data matrix  $A$  will have a block-wise Hankel matrix structure with many of its entries from same  $k$ -space locations being repeated in anti-diagonal directions (emphasized by colored samples in Fig. 1a). We define the following linear operator that generates a data matrix from a multi-channel dataset.

$$H := \mathbb{C}^{N_x \times N_y \times N_c} \rightarrow \mathbb{C}^{w^2 N_c \times (N_x - w + 1)(N_y - w + 1)} \quad [7]$$

Then a reverse (not inverse) operator that generates a corresponding  $k$ -space dataset from a data matrix (possibly without a structure) would be

$$H^\dagger := \mathbb{C}^{w^2 N_c \times (N_x - w + 1)(N_y - w + 1)} \rightarrow \mathbb{C}^{N_x \times N_y \times N_c}, \quad [8]$$

where  $\dagger$  denotes a pseudo-inverse operator. This operation is equivalent to averaging the anti-diagonal entries, and putting them in appropriate  $k$ -space locations. We also define a projection operator ( $P_{HH^\dagger}$ ) that projects a data matrix onto the space of block-wise Hankel matrices.

$$P_{HH^\dagger} := HH^\dagger, \quad [9]$$

### Parallel Imaging Reconstruction as a Low-rank Matrix Completion

So far, our discussion assumed that we have auto-calibration signal to extract subspace information from. However, when the under-sampled dataset does not have ACS, then we cannot estimate the basis that spans the signal subspace from the calibration matrix. In Fig. 1b, a SSoS-combined, center  $30 \times 30$  portion of the under-sampled brain data (bottom) is shown with its corresponding singular value plot (dashed) in Fig. 1c. The under-sampled data has been generated retrospectively using a uniform Poisson-disc (19)

random sampling pattern with an overall acceleration factor of five. As seen in Fig. 1c, now the under-sampled calibration matrix no longer has low rank and we cannot identify dominant left singular vectors that would span the signal subspace. Since the estimation of the basis that spans the signal subspace is not possible, previously discussed subspace-based calibration consistency condition cannot be formulated. Instead, we turn to the information that the signal subspace has low dimension or, equivalently, that the signal matrix has low rank.

Our approach in formulating SAKÉ is to recover the low-rank signal matrix  $S$  when only a subset of entries in  $A$  is given due to under-sampling in  $k$ -space. Let  $\Omega$  be a subset of the complete set of entries  $\{1, \dots, m\} \times \{1, \dots, n\}$  that represents a sampling pattern in a data matrix. Then a linear operator that selects only the acquired entries in the data matrix can be defined as the following:

$$P_{\Omega}(X) : \mathbb{C}^{m \times n} \rightarrow \mathbb{C}^{m \times n}, \quad \begin{aligned} X(i, j) &= X(i, j), & \text{if } (i, j) \in \Omega \\ X(i, j) &= 0, & \text{if } (i, j) \notin \Omega \end{aligned} \quad [10]$$

With Eq. 9 and 10, the parallel imaging reconstruction can be formulated into a structured low-rank matrix completion problem.

$$\begin{aligned} &\underset{X}{\text{minimize}} \quad \|P_{\Omega}P_{HH^{\dagger}}(A - X)\|_F^2 \\ &\text{subject to} \quad \text{rank}(X) = k. \end{aligned} \quad [11]$$

In other words, we look for a low-rank matrix  $X$  (low-rankness) of which its block-wise Hankel matrix approximation ( $P_{HH^{\dagger}}$ , structural consistency) is consistent with the data matrix  $A$  on the set of acquired entries ( $P_{\Omega}$ , data consistency). Note that for the under-sampled data matrix  $A$ , the relation  $P_{\Omega}P_{HH^{\dagger}}A = A$  holds.

The optimization in Eq. 11 is performed on the data matrix. It is much more convenient to change variables and recast the problem to solve for  $k$ -space directly:

$$\begin{aligned} &\underset{x}{\text{minimize}} \quad \|(Dx - y)\|^2 + \lambda R(x) \\ &\text{subject to} \quad \text{rank}(X) = k, \quad x = H^{\dagger}(X). \end{aligned} \quad [12]$$

Here,  $D$  is an operator that selects acquired  $k$ -space locations and  $H^{\dagger}$  (Eq. 8) converts data matrix into  $k$ -space. Also,  $R(x)$  is an additional regularization term that enforces *a priori* information to the reconstructed data, and  $\lambda$  is a parameter that finds a balance between the data consistency and the *a priori* penalty. For convenience, we assume the

data has been pre-whitened. Again, we search for a low rank matrix  $X$  (low-rankness), which, when transformed into  $k$ -space data  $x$  (structural consistency), is consistent with the acquired data  $y$  (data consistency) at the sampled locations chosen by  $D$ . It is worthwhile noting that the formulation in Eq. 11 is similar to the low-rank matrix completion setup in (12). Our case differs in the sense that we also enforce a block-Hankel structure in the matrix. This significantly reduces the degrees of freedom in the reconstruction and makes the solution more tractable. Additionally, the (random) under-sampling pattern is no longer defined in data matrix domain. In MRI experiments, sampling patterns are defined in  $k$ -space and are equivalent for all the channels. The consequence is that a *pseudo*-random pattern will repeatedly show up across multiple rows of the data matrix (Fig. 3) and that a *purely* random pattern over the entire entries of the data matrix is not achievable.

### **Iterative Reconstruction**

Although many possible ways to solve Eq. 12 exist, such as minimum nuclear norm method (12), we take a simple iterative projection-onto-sets type approach similarly to the well-known Cadzow algorithm (20). We replace the data consistency term with the data equality constraint ( $Dx = y$ ) and iteratively enforce: 1) low-rankness in the data matrix constructed from the current estimate of  $k$ -space data by hard-thresholding singular values, 2) block-wise Hankel structural consistency by transforming the low-rank data matrix back into a multi-channel dataset, and 3) data equality constraint by replacing estimates of  $k$ -space samples with acquired data at sampled locations. The iteration persists until some convergence criteria are met. Optionally, when *a priori* information about underlying MR signal is given, the regularization can easily be added into the reconstruction process. Illustration of the proposed algorithm is shown in Fig. 3.

### **Parameter Selection**

There are three things that need to be decided before performing the SAKÉ reconstruction: sampling pattern, window size, and rank value. A great body of work in matrix completion focuses on sampling the entries of the data matrix randomly (12). To mimic this condition, we have confined all of our experiments to adopt *pseudo*-random

under-sampling in  $k$ -space. This approach has an additional benefit of having incoherent, noise-like artifacts, as opposed to having coherent aliased objects resulting from uniform under-sampling, in the final reconstructed images. This is similar to the case of compressed sensing where random sampling causes very incoherent aliasing that spreads uniformly to other image pixels. Additionally, we retained the center  $4 \times 4$  fully sampled data for faster convergence. The argument for choosing the window size is similar to other auto-calibrating methods (7, 8). As with any subspace method, too small of a window size will not capture the entire subspace, and too large window will add instability and additional computational complexity. We found that window size of  $6 \times 6$  to  $9 \times 9$  works well for most coil array geometries. These sizes are also consistent with GRAPPA and SPIRiT. The actual rank of the data matrix depends on the number of coils, the correlations between the coil sensitivity functions and the actual size of the object within the supported FOV. However, as opposed to sensitivity maps that could change based on loading and placement, we found that the rank value of the data matrix does not change as much. Here, we first estimated the rank value empirically from the full data and then used it repeatedly over the experiments. In other scenarios, the rank can be estimated from a short pre-scan and be used subsequently in the reconstruction.

## **MATERIALS AND METHODS**

### **Multi-channel MR Data**

The brain image of a healthy volunteer was acquired through a  $T_1$ -weighted, 3D spoiled gradient echo (SPGR) sequence. Scan parameters were set to TE = 8 ms, TR = 17.6 ms, and flip angle =  $20^\circ$ . Imaging parameters were chosen such that field of view (FOV) = 20 cm  $\times$  20 cm  $\times$  20 cm with a matrix size of  $200 \times 200 \times 200$  for an isotropic 1 mm<sup>3</sup> resolution. A single slice was selected from this data set and was used through out the experiments. The scan was performed on a 1.5T MRI scanner (GE, Waukesha, WI) using an 8-channel receive-only head coil. In demonstrating non-Cartesian reconstruction capability, we used a phantom data acquired with a spiral gradient echo sequence using an 8-channel cardiac coil. The spiral trajectory consists of 60 interleaves for 0.75 mm in-

plane resolution over a 30 cm x 30 cm FOV. Both of the data sets can be found in the SPIRiT package on-line (<http://www.eecs.berkeley.edu/~mlustig/Software.html>).

### Convergence Behavior

Three different *pseudo*-random under-sampling patterns were generated to test convergence behavior of the proposed algorithm: uniform random under-sampling, uniform Poisson-disc random under-sampling, and variable-density (VD) Poisson-disc random under-sampling (19). Full brain data was retrospectively under-sampled with each sampling pattern and reconstruction ran over 50 iterations. During iterations, normalized root mean squared error (nRMSE) of the current estimate ( $\tilde{x}$ ) with respect to fully sampled reference ( $x$ ) was calculated in image domain and was plotted as a function of iterations.

$$\text{nRMSE} = \frac{\sqrt{\sum_{i=0}^{N-1} (x(i) - \tilde{x}(i))^2}}{N \cdot \max(x) - \min(x)} \quad [13]$$

In all three cases, data matrices were constructed using a  $6 \times 6 \times 8$  window and 55 (out of 288) singular values were kept at each iteration for singular value hard-thresholding.

### Comparison to SPIRiT

A calibrationless reconstruction method should produce a comparable reconstruction result when an under-sampled data set with ACS is given, and have the additional feature to handle a data set without ACS. Based on this reasoning, we compared the reconstruction performance of SAKÉ to SPIRiT. For this particular data set, it was shown in (8) that SPIRiT outperforms GRAPPA.

A VD Poisson-disc random sampling pattern with 5-fold acceleration was prepared to make two sampling patterns that have  $30 \times 30$  ACS and  $4 \times 4$  fully sampled region in the origin of  $k$ -space. First, the brain data set was under-sampled with the sampling pattern that had  $30 \times 30$  ACS and was reconstructed using both SPIRiT and SAKÉ. Then, for comparison, we performed another SAKÉ reconstruction using the under-sampled data that had  $4 \times 4$  fully sampled center. Finally, in order to cope with the longer

reconstruction time of SAKÉ, a hybrid method utilizing both the SAKÉ and SPIRiT reconstruction was tested. In this scheme, SAKÉ was employed to generate a  $30 \times 30$  calibration data for SPIRiT from under-sampled data without ACS. Once the calibration data is given, SPIRiT can perform its normal reconstruction procedures to produce a reconstructed full data set. This hybrid method inherits advantages from both the methods. For the case of SPIRiT, a projection-onto-convex-sets (POCS) module was used with Tychonov regularization parameter value of 0.01, kernel size of  $7 \times 7$  for data calibration and the reconstruction ran for 20 iterations. In the SAKÉ reconstruction, a smaller window of  $6 \times 6 \times 8$  was used in generating the data matrix for faster reconstruction and 55 dominant singular values were kept at each iterations. In the reconstructions, the number of iterations was fixed to 30.

### **Combination with Compressed Sensing**

It is well known that MR images have sparse representation (13) in some transform domain (ex. wavelet). In order to demonstrate the regularization capability of SAKÉ, we adopted the joint sparsity model (19), an assumption that multi-channel images are jointly sparse, and added the following generalized  $\ell_1$ -norm penalty term into the optimization Eq. 12.

$$R(x) = \sum_r \sqrt{\sum_c |\Psi\{IFFT(x)\}|^2} \quad [14]$$

Here,  $\Psi$  denotes a wavelet transform of an MR image with  $r$  and  $c$  indexing the spatial and coil dimension, respectively. In the iterative reconstruction, the aforementioned penalty has been implemented as iterative soft-thresholding on the transform coefficients.

### **Non-Cartesian Multi-channel Reconstruction**

To demonstrate non-Cartesian reconstruction capability, we have under-sampled the spiral data set by a factor of three to have 20 equally spaced interleaves. The under-sampled data set was reconstructed using gridding with density compensation and SAKÉ reconstruction. For fast gridding, we have adopted the non-uniform FFT (NUFFT) package (21). In the SAKÉ reconstruction, data consistency was enforced in the non-uniformly sampled  $k$ -space domain. We used the LSQR algorithm (22) to implement inverse-NUFFT operation within the iterative reconstruction. The reconstruction ran over

30 iterations keeping 45 dominant singular values each iteration and a  $260 \times 360$  sized final image was generated.

### **Hardware and Software**

We used Matlab (The Math Works, Inc.) to implement SAKÉ. In the spirit of reproducible research, we provide implementations of the algorithms and examples demonstrating its use. These can be found in (<http://www.eecs.berkeley.edu/~mlustig/Software.html>). All the programs were run on a Linux machine equipped with an Intel i7-2600K, 3.40GHz CPU and 12 gigabytes of memory.

## **Results**

### **Convergence Behavior**

Three different sampling patterns used in this experiment are shown in Fig. 4b: uniform random (top), uniform Poisson-disc (middle), and VD Poisson-disc (bottom). Each sampling pattern achieved an acceleration factor of three. As shown in Fig. 4c, we have observed significantly distinct convergence behaviors between the sampling patterns. VD Poisson-disc nearly reached its optimum (minimum nRMSE) solution after 20 iterations, whereas uniform random sampling is far from converging even after 50 iterations. Based on the faster convergence characteristic, we have adopted VD Poisson-disc sampling pattern for all of the following experiments. Note that the reconstruction result from uniform random sampling has larger residual aliasing artifacts (Fig. 4d) than the VD-Poisson disc.

### **Comparison to SPIRiT**

The 5-fold accelerated sampling patterns with  $30 \times 30$  ACS and  $4 \times 4$  fully sampled center is shown in Fig. 5a. Relative data acquisition time in adopting each patterns are calculated in Table 1. Fig. 5b shows a series of reconstruction (top row) and error (bottom row) results generated from applying different reconstruction methods. Given the same amount of data with  $30 \times 30$  ACS, SAKÉ produces a comparable reconstruction

result to SPIRiT. Moreover, even with less information provided by the under-sampling without ACS, SAKÉ still reconstructs good quality images with no observable artifacts. Finally, the reconstruction result of applying the hybrid method shows that SAKÉ can be utilized to reconstruct calibration data for other auto-calibrating methods. In this way, data acquisition time can be further reduced by not acquiring fully sampled center regions in  $k$ -space at the expense of slight increase in reconstruction time spent in ACS reconstruction. Relative reconstruction times when employing the different methods are shown in Table 1.

### **Combination with Compressed Sensing**

Fig. 6a and 6d shows SAKÉ reconstruction results without and with a  $\ell_1$ -norm penalty, respectively, from the 3-fold accelerated sampling pattern. The zoomed images (Fig. 6b and 6c) clearly show the effect of applying an additional sparsity constraint, which suppresses the over-fitting to noise in the acquired data.  $\lambda$  value was set empirically to 0.007. Choosing smaller  $\lambda$  values would result in images with more noise and applying large  $\lambda$  values might destroy fine structures in reconstructed images.

### **Non-Cartesian Multi-channel Reconstruction**

Fig. 7 shows a fully sampled spiral acquisition image (a), 3-fold under-sampled gridding reconstructed image (b), and 3-fold under-sampled SAKÉ reconstructed image (c). By comparing (b) and (c), we can clearly see that aliasing artifacts have been removed by SAKÉ reconstruction. It is worth mentioning that a data matrix constructed from a gridded full data set also showed low-rankness with 45 to 50 dominant singular values.

## **Discussion**

In general, auto-calibrating parallel imaging reconstructions are done in two steps: a calibration process followed by data interpolation. The calibration step is where either linear weights relating blocks of  $k$ -space data or explicit sensitivity estimation is done using ACS in the center of acquired  $k$ -space data. Once the calibration information is extracted, it is used in the data reconstruction step where missing  $k$ -space samples are



interpolated. In the SAKÉ method developed in this project, calibration is done implicitly by enforcing the data matrix to be a structured low rank matrix. As a result of sensitivity encoding, any (vectorized) blocks of  $k$ -space data lie in a low dimensional subspace, which we called a signal subspace. Here, we have shown that calibration can be done without explicitly extracting the coil information by exploiting the low dimensionality of the signal subspace.

The sampling patterns in  $k$ -space have a significant impact on the SAKÉ reconstruction. As the overall mathematical formulation of restricting the rank of data matrix is not convex, it is crucial that we start the reconstruction with an initial estimate (usually, this is the under-sampled data itself) that lies close to the global optimum to ensure a fast convergence. Our approach in securing a convergence to the global optimum with reasonable reconstruction time was to make sure that a small fraction of the origin of  $k$ -space is sampled. In all of our observations,  $2 \times 2$  full sampling was enough to ensure the convergence for many sampling patterns, and  $4 \times 4$  was adopted for a faster convergence. We would like to point out that with  $4 \times 4$  full sampling, reconstruction with regular uniform under-sampling was also possible (data not shown). Other approaches that adopt convex relaxation to the low-rank matrix completion, for example minimizing nuclear-norm of the data matrix (12), might be possible though we have not tested it thoroughly. The window size in constructing a data matrix has an effect on the quality of the reconstructed images. Using larger windows may benefit higher acceleration reconstruction at the cost of increased computational load. We have found that a  $6 \times 6$  sized window is enough for reconstructing a 5-fold acceleration data set with the 8-channel coil we used. However, any window size smaller than  $6 \times 6$  would result in final images with residual aliasing. The size of the window can be adapted to different coil geometries, similarly to kernel size selection in GRAPPA.

The specific rank value for hard-thresholding can be estimated from a separate scan prior to the actual data acquisition. However, when rank estimation is not possible, a greedy approach can be adopted. In other words, we can start the SAKÉ reconstruction by setting a lower rank and increase it over the iterations until some convergence criteria is met. Further research on the behavior of the rank in relation to changes of imaging subject, coil geometries, and other factors in data acquisition remains as a future work.

Most of the reconstruction time in SAKÉ is spent in performing SVD on the large data matrix in every single loop. The computational complexity will increase with a higher rank value, larger window size, and large image size. To reduce the computational load, one could adopt faster SVD implementations such as PROPACK (23) that computes a few singular values and corresponding singular vectors based on Lanczos bidiagonalization. Adopting GPU-based computing (24) is also a possibility. Other approaches in reducing the reconstruction time include using SAKÉ to reconstruct only the calibration data as shown in Fig. 5. Once the calibration data is at hand, many other auto-calibrating methods can be adopted for full data reconstruction.

In some ways, the iterative iGRAPPA algorithm (25) is similar to SAKÉ. In iGRAPPA, a new GRAPPA kernel is calibrated every iteration from the reconstructed data and then applied to obtain a better approximation. Calibrating a new kernel is similar to learning the low dimensional signal subspace. Our approach is more general as it captures the entire signal subspace using the SVD.

## **Conclusions**

In this work, we have presented a calibration data-free, auto-calibrating parallel imaging reconstruction method called SAKÉ. The proposed method formulates the parallel imaging reconstruction as a structured low-rank matrix completion problem and solves it by iteratively enforcing multiple consistencies (which can include sparsity). We have shown that SAKÉ can produce comparable results to SPIRiT in terms of accurate de-aliasing and noise performance. Lastly, the reconstruction with non-Cartesian data shows the flexibility of SAKÉ.

## **Acknowledgements**

The authors thank Dr. Cornelius Von Morze, Dr. Martin Uecker and Dr. Bart Vandereycken for helpful discussions. This study was supported by NIH grants P41 EB013598, R01 EB009690, P41 RR09784, R00 EB012064, American Heart Association 12BGIA9660006, UC Discovery – ITLbio 178688, and GE Healthcare.

## Table

Table 1. Relative data acquisition time and reconstruction time in adopting different sampling patterns and varying reconstruction methods. Acquisition time is given as the number of samples acquired.

	30 × 30 SPIRiT	30 × 30 SAKÉ	4 × 4 SAKÉ	4 × 4 SAKÉ / SPIRiT
Acquisition Time (samples)	8784	8784	8002	8002
Reconstruction Time (sec)	5	520	508	42

## References

1. Larkman DJ, Nunes RG. Parallel magnetic resonance imaging. *Phys Med Biol* 2007;52:15-55.
2. Sodickson DK, Manning WJ. Simultaneous acquisition of spatial harmonics (SMASH): fast imaging with radiofrequency coil arrays. *Magn Reson Med* 1997;38:591-603.
3. Pruessmann KP, Weiger M, Scheidegger MB, Boesiger P. SENSE: Sensitivity encoding for fast MRI. *Magn Reson Med* 1999;42:952-962.
4. Blaimer M, Breuer F, Mueller M, Heidemann R, Griswold MA, Jacob P. SMASH, SENSE, PILS, GRAPPA: how to choose the optimal method. *Top Mag Reson Imaging* 2004;15:223-236.
5. Ying L, Sheng J. Joint image reconstruction and sensitivity estimation in SENSE (JSENSE). *Magn Reson Med* 2007;57:1196-1202.
6. Uecker M, Hohage T, Block KT, Frahm J. Image reconstruction by regularized nonlinear inversion: application to autocalibrated parallel imaging. *Magn Reson Med* 2008;60:674-682.
7. Griswold MA, Jakob PM, Heidemann RM, Nittka M, Jellus V, Wang J, Kiefer B, Haase A. Generalized autocalibrating partially parallel acquisitions (GRAPPA). *Magn Reson Med* 2002;47:1202-1210.
8. Lustig M, Pauly JM. SPIRiT: iterative self-consistent parallel imaging reconstruction from arbitrary  $k$ -space. *Magn Reson Med* 2010;64:457-471.
9. Zhang J, Liu C, Moseley ME. Parallel reconstruction using null operators. *Magn Reson Med* 2011;66:1241-1253.
10. Lustig M, Elad M, Pauly JM. Calibrationless Parallel Imaging Reconstruction by Structured Low-Rank Matrix Completion. In:

- Proceedings of the 18th Annual Meeting of ISMRM, Stockholm, 2010. p 2870.
11. Lustig M. Post-Cartesian Calibrationless Parallel Imaging Reconstruction by Structured Low-Rank Matrix Completion. In: Proceedings of the 19th Annual Meeting of ISMRM, Montreal, 2011. p 483.
  12. Candés EJ, Plan Y. Matrix completion with noise. *Proc IEEE* 2010;98(6):925-936.
  13. Lustig M, Donoho DL, Pauly JM. Sparse MRI: the application of compressed sensing for rapid MR imaging. *Magn Reson Med* 2007;58:1182-1195.
  14. Noll DC, Nishimura DG, Macovski A. Homodyne detection in magnetic resonance imaging. *IEEE Trans Med Imaging* 1991;10:154–163.
  15. Van Der Veen A-J, Deprettere EF, Swindlehurst AL. Subspace-based signal analysis using singular value decomposition. *Proc IEEE* 1993;81(9):1277-1308.
  16. Golub GH, Van Loan CF. *Matrix Computations*. The Johns Hopkins University Press, 3<sup>rd</sup> edition 1996.
  17. Ipsen ICF. *Numerical matrix analysis: linear systems and least squares*. Society for Industrial and Applied Mathematics, 2009.
  18. Lustig M, Lai P, Murphy M, Vasanawala SM, Elad M, Zhang J, Pauly JM. An Eigen-Vector Approach to AutoCalibrating Parallel MRI, Where SENSE Meets GRAPPA. In: Proceedings of the 19th Annual Meeting of ISMRM, Montreal, 2011. p 479.
  19. Vasanawala S, Murphy MJ, Alley MT, Lai P, Keutzer K, Pauly JM, Lustig M. Practical parallel imaging compressed sensing MRI: Summary of two years of experience in accelerating body MRI of pediatric patients. *IEEE International symposium on biomedical imaging: From nano to macro* 2011:1039-1043.
  20. Cadzow JA. Signal enhancement - a composite property mapping algorithm. *IEEE Trans Acoust, Speech, Signal Process* 1988;36:49-62.
  21. Fessler J, Sutton B. Nonuniform fast Fourier transform using min-max interpolation. *IEEE Trans Signal Process* 2003;51:560-574.
  22. Paige Cc, Saunders MA. LSQR: An algorithm for sparse linear equations and sparse least-squares. *TOMS* 1982;8:43-71.
  23. Larsen RM. Lanczos bidiagonalization with partial reorthogonalization. *DAIMI PB-357* 1998.
  24. Murphy M, Alley M, Demmel J, Keutzer K, Vasanawala S, Lustig M. Fast  $\ell_1$ -SPIRiT Compressed Sensing Parallel Imaging MRI: Scalable Parallel Implementation and Clinically Feasible Runtime. *IEEE Trans Med Imag* 2012;31(6):1250-1262.
  25. Zhao T, Hu X. Iterative GRAPPA (iGRAPPA) for improved parallel imaging reconstruction. *Magn Reson Med* 2008;59:903-7.

## Figure Legends

Figure 1: Constructing a data matrix from a multi-channel  $k$ -space dataset and effect of under-sampling on singular values. a) A single data block in the  $k$ -space is vectorized into a column in the data matrix. Note that any data matrix generated in this way will have a block-wise Hankel matrix structure. b) SSoS combined images of full (top) and randomly under-sampled (bottom)  $30 \times 30$  calibration data. c) Singular values of data matrices constructed with the full and under-sampled calibration data. The data matrix from the fully sampled data has rapidly decaying singular values and can be well approximated by a low rank matrix. Note that ranges of the singular values of the full (left scale) and under-sampled (right scale) data are different due to the effect of under-sampling.

Figure 2: Depiction of subspace separation by singular value hard-thresholding. a) Magnitude images of a single channel (top row) and SSoS combined images (bottom row) corresponding to full data (left column), signal subspace (middle column), and noise subspace (right column) are shown. The subspace separation by setting rank equal to 55 clearly shows de-noising effect of the singular value thresholding operation. The images corresponding to the noise subspace has been multiplied by a factor of 10 for visualization. All images within the same rows share the same display ranges, except the noise subspace images have been multiplied by a factor of 10 for visualization. b) Visualization of the noise subspaces with varying rank values. White arrows point to residual signals left in the noise subspaces due to under-estimating the rank value.

Figure 3: Diagram of iterative reconstruction in SAKÉ. Within a single iteration, multiple consistencies are enforced on current estimate of the  $k$ -space data. As under-sampling is done the same for all channels, a *pseudo*-random sampling pattern (white circles) appears repeatedly in the data matrix.

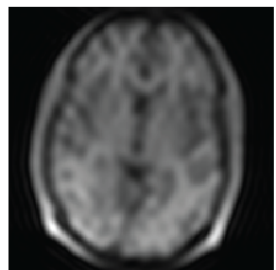
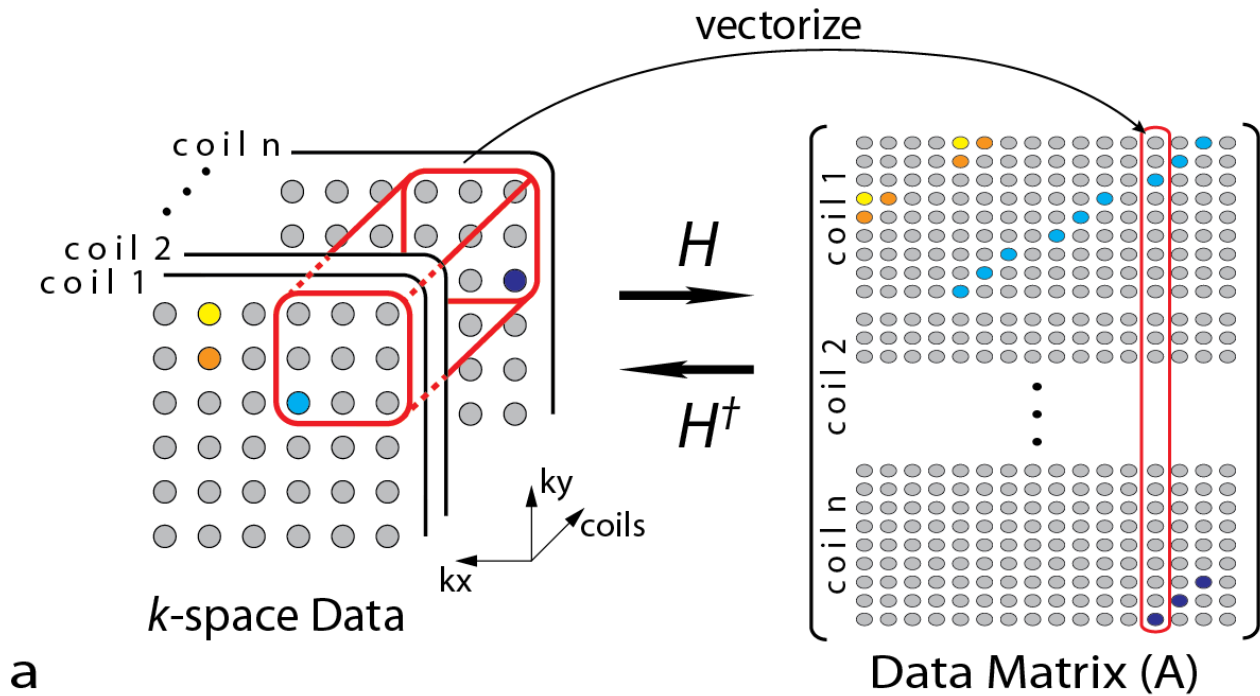
Figure 4: Reconstruction results of multi-channel brain image with different random under-sampling patterns. a) Full data combined using SSoS. b) Sampling patterns used to under-sampled the data set. Uniformly random (Top), uniform Poisson-disc random

(Middle), and variable density Poisson-disc random (Bottom) patterns are shown. c) Convergence profile depicted by normalized root-mean-squared-error (nRMSE) as a function of number of iterations. The variable density Poisson-disc random sampling shows the fastest convergence, nearly reaching its minimum error (marked by the asterisk) within 20 iterations. d) Reconstruction results and error images for the random sampling patterns. The uniform random sampling has the most residual aliasing artifacts left in its final reconstructed image.

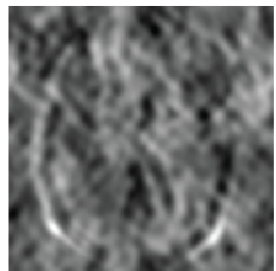
Figure 5: Reconstruction performance of SAKÉ compared to SPIRiT. a) A factor-of-5 acceleration sampling with a  $30 \times 30$  ACS (Top) and  $4 \times 4$  fully sampled origin (Bottom). b) Reconstruction results of SAKÉ and SPIRiT for the different sampling patterns. Overall, SAKÉ shows good reconstruction performance comparable to that of SPIRiT even without ACS. The rightmost result shows that SAKÉ can be adopted to reconstruct a full ( $30 \times 30$ ) ACS for other auto-calibrating reconstruction methods.

Figure 6: Regularization using  $\ell_1$ -wavelet spatial sparsity with 3-fold acceleration. a) SSoS combined image with no regularization. b) and c) are magnified versions of square boxes in a) and d), respectively. d) SSoS combined image with  $\ell_1$ -wavelet (Daubechies 4) regularization. Note that the images without regularization are much more grainy, while fine spatial features are well preserved with regularization.

Figure 7: SAKÉ reconstruction results of non-Cartesian parallel imaging. a) Fully sampled, and b) 3-fold under-sampled spiral phantom images gridded and SSoS combined. c) SAKÉ reconstruction result using 3-fold under-sampling with data consistency applied on the non-Cartesian  $k$ -space samples, which removed the aliasing artifacts as compared to b).



Full Calibration Data



Under-sampled Calibration Data

b

Singular Values

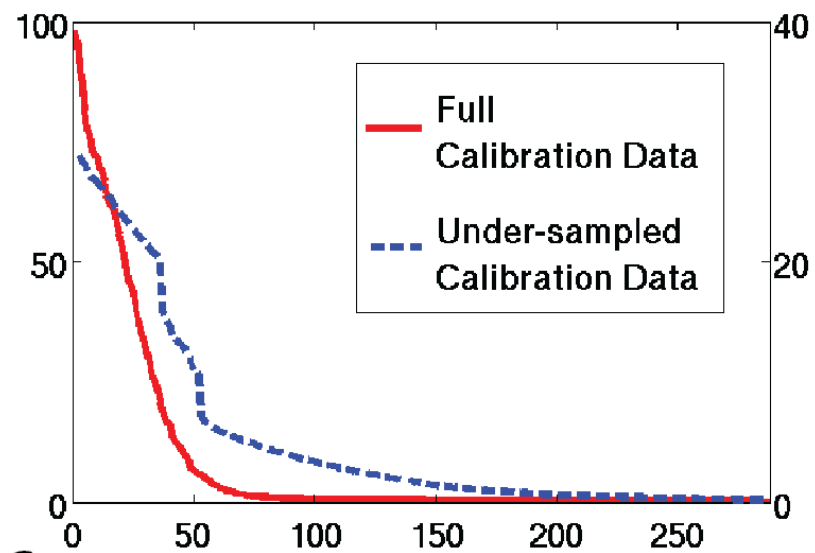


Figure 1

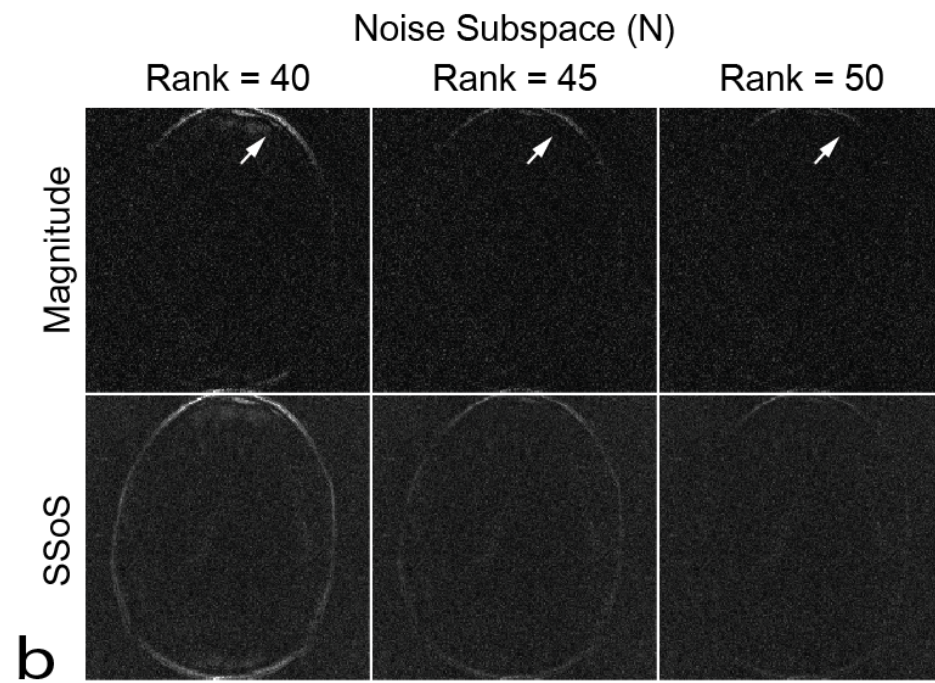
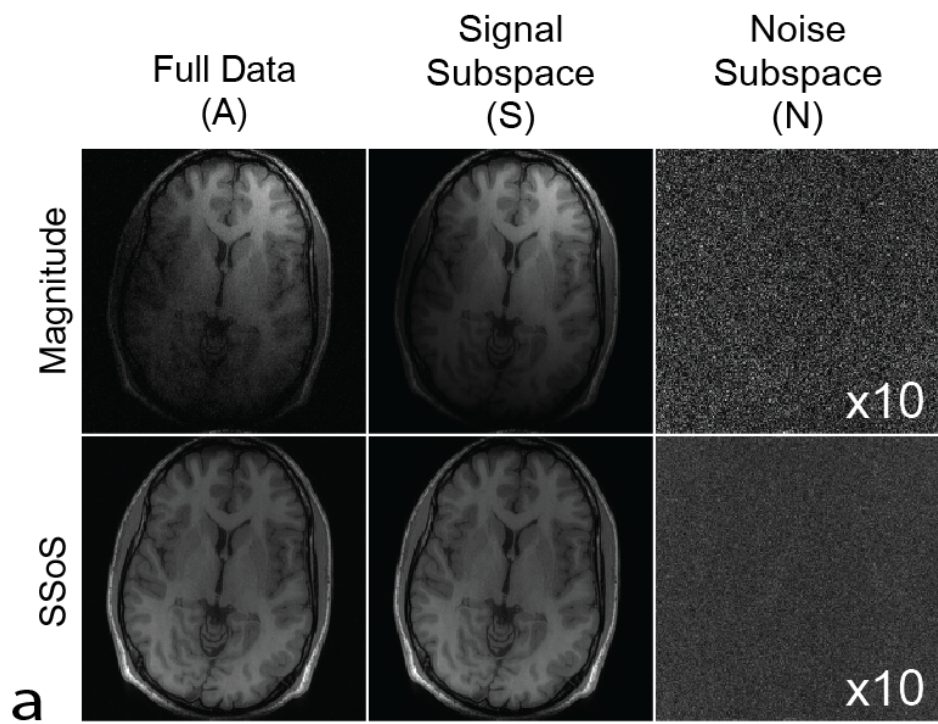


Figure 2



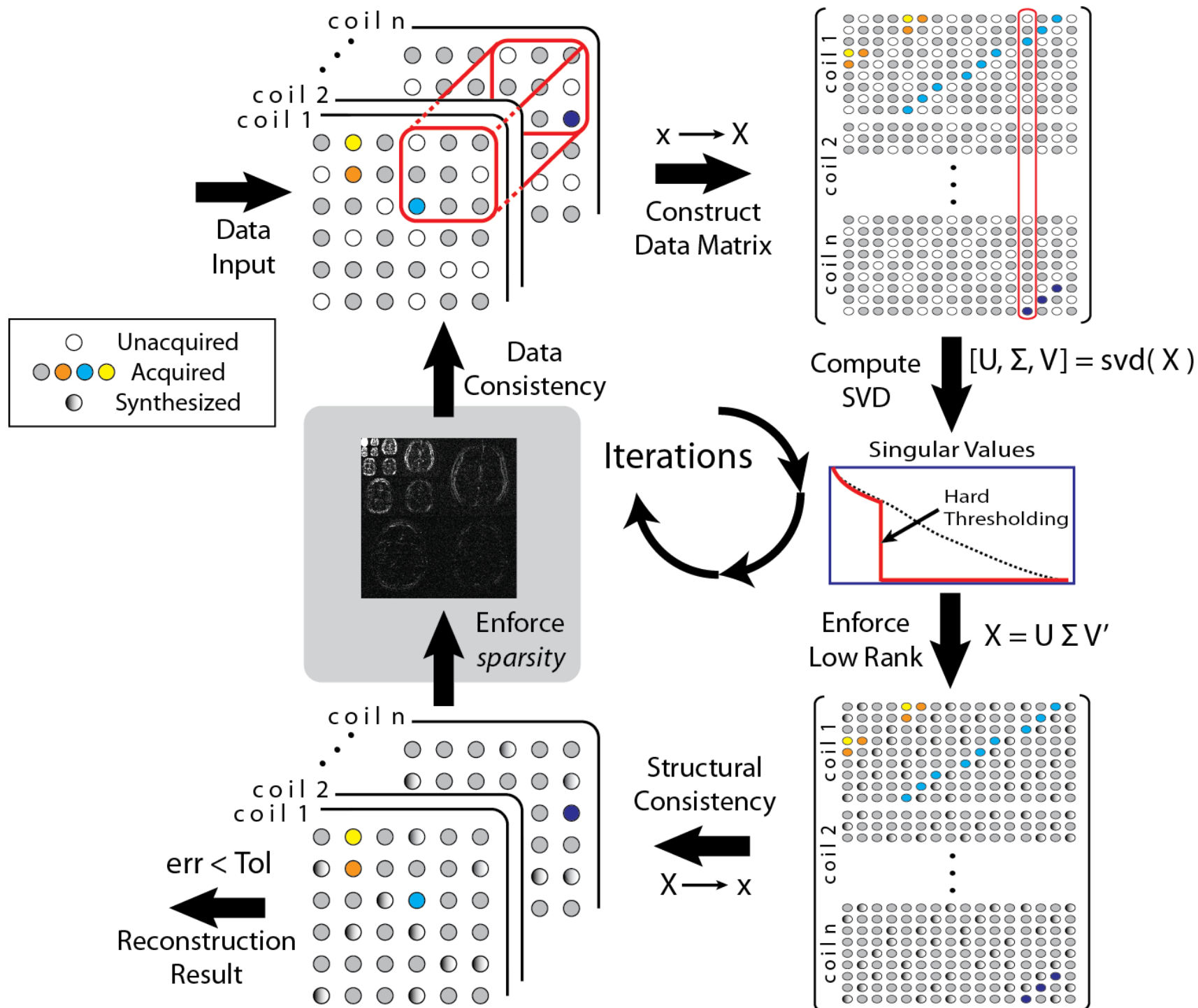


Figure 3

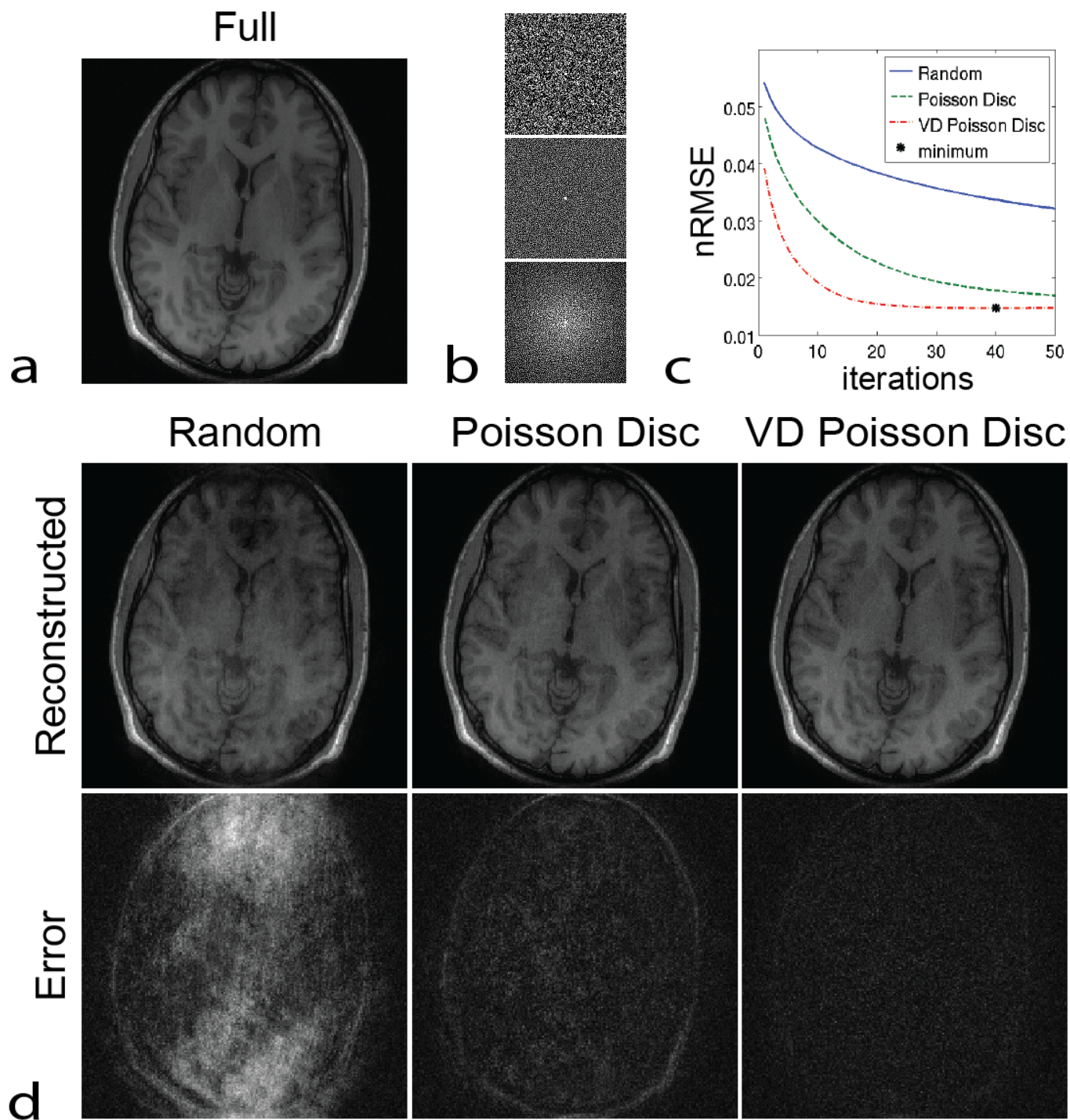


Figure 4

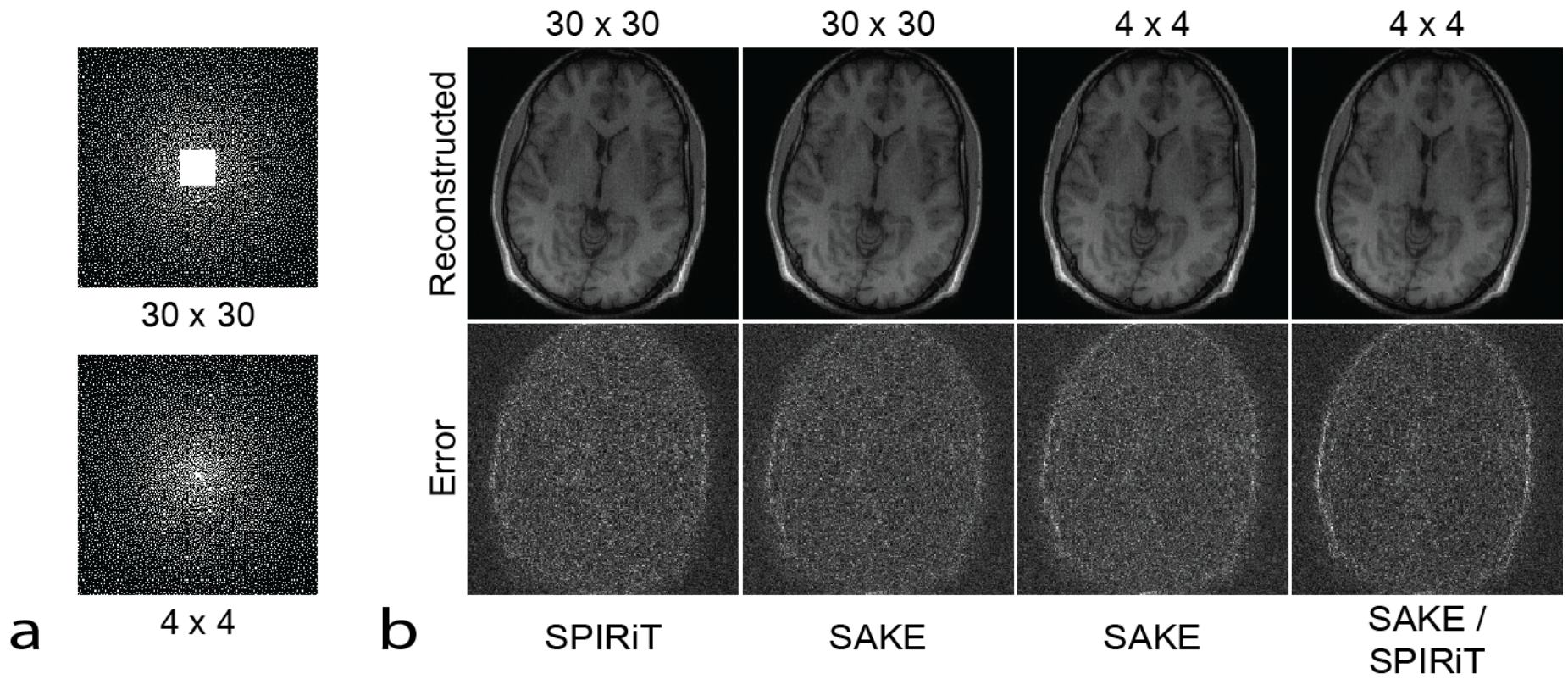


Figure 5



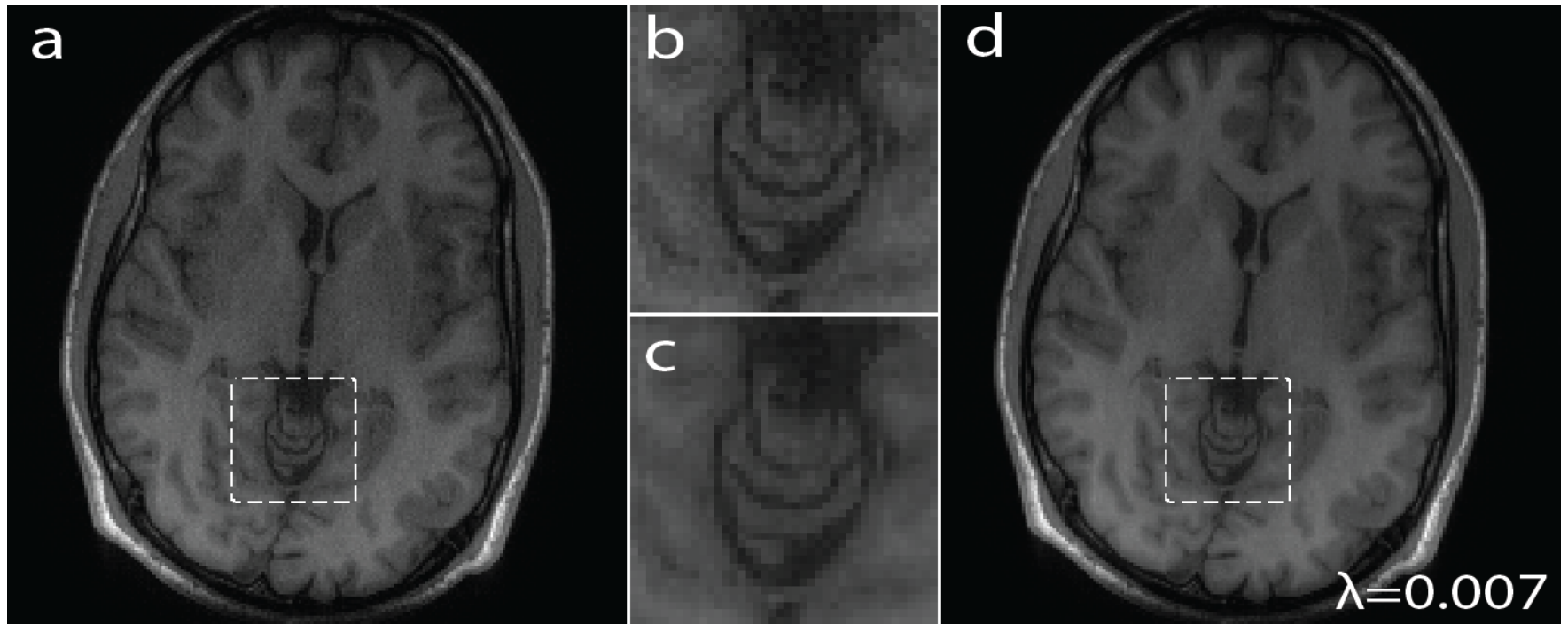


Figure 6

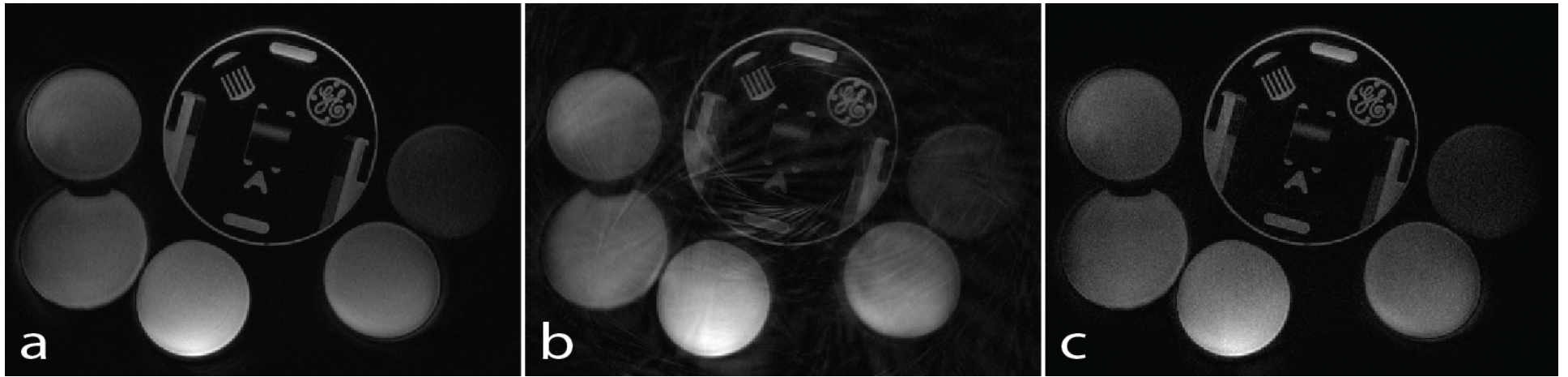


Figure 7